Developing Thin-Film-Composite Forward Osmosis Membranes on the PES/SPSf Substrate Through Interfacial Polymerization

Kai Yu Wang and Tai-Shung Chung
Dept. of Chemical and Biomolecular Engineering, National University of Singapore, Singapore 117576

Gary Amy
Water Desalination and Reuse (WDR) Center, King Abdullah University of Science and Technology, Thuwal 23955-6900, Saudi Arabia

DOI 10.1002/aic.12635
Published online April 22, 2011 in Wiley Online Library (wileyonlinelibrary.com).

A new scheme has been developed to fabricate high-performance forward osmosis (FO) membranes through the interfacial polymerization reaction on porous polymeric supports. p-*Phenylenediamine and 1,3,5-trimesoylchloride were adopted as the monomers for the in-situ polycondensation reaction to form a thin aromatic polyamide selective layer of 150 nm in thickness on the substrate surface, a lab-made polyethersulfone (PES)/sulfonated polysulfone (SPSf)-alloyed porous membrane with enhanced hydrophilicity. Under FO tests, the FO membrane achieved a higher water flux of 69.8 LMH when against deionized water and 25.2 LMH when against a model 3.5 wt % NaCl solution under 5.0 M NaCl as the draw solution in the pressure-retarded osmosis mode. The PES/SPSf thin-film-composite (TFC)-FO membrane has a smaller structural parameter* S *of 238 μm than those reported data. The morphology and topology of substrates and TFC-FO membranes have been studied by means of atomic force microscopy and scanning electronic microscopy.* © 2011 American Institute of Chemical Engineers *AIChE J,* 58: 770–781, 2012

Keywords: forward osmosis, desalination, interfacial polymerization, membrane, thin-film-composite

Introduction

Nowadays, fresh water scarcity is perhaps the most serious constraint to sustainable development, particularly in drought-prone and environmentally polluted areas. To solve or alleviate the global water scarcity problem, tremendous efforts have been made to identify novel technologies for seawater desalination and wastewater reclamation at reduced energy consumptions.[1,2] Membrane-based separation processes have advantages of avoiding thermally imposed efficiency limitations on heat consumption compared to thermal-based separation processes. There are distinguished different driving forces to accomplish various membrane separations. For example, the reverse osmosis (RO) polymeric membrane for desalination uses high-hydraulic pressures as the driving force. Recently, the forward (direct) osmosis (FO) process, which uses osmotic pressures as the driving force, represents an emerging membrane technology. The unique characteristics of no or low-hydraulic pressure operation in FO processes have attracted considerable attentions in various fields including wastewater treatment,[3,4] seawater desalination,[5–8] pharmaceutical and juice concentration,[9,10] power generation,[11–13] and protein enrichment.[14]

Correspondence concerning this article should be addressed to T.-S. Chung at chencts@nus.edu.sg.

In an FO process, the osmotic pressure gradient between the concentrated draw solution and the saline feed supplies a spontaneous driving force for water transport.[15] The osmotic pressures provided in FO can be significantly higher than hydraulic pressures used in RO as the driving force, subsequently resulting in a higher theoretical water flux. Moreover, FO may offer the advantages of higher rejections to a wide range of contaminants and lower membrane-fouling propensities compared to traditional pressure-driven membrane processes.[4,16–19] However, a fundamental hurdle that deters the successful implementation of this innovative process is the lack of tailored membranes with the appropriate separation performance.

Similar to the RO process, the FO process utilizes semipermeable membranes to induce separating water from dissolved solutes. To develop these polymeric semipermeable membranes, mainly two different fabrication techniques have been adopted: (1) asymmetric membranes made by the nonsolvent induced wet-phase inversion approach,[20–25] and (2) thin-film-composite (TFC) membranes made by interfacial polymerization (IP).[26–28] TFC membranes made of aromatic polyamide (PA) have dominated RO membrane development, as it was invented in 1970s.[29–35] TFC membranes are synthesized via the in situ IP reaction between two monomer solutions; namely, an aqueous polyfunctional amine solution and a polyfunctional acyl chloride dissolved in an apolar organic solvent. Because of the solubility preference of monomers in two different phases, immiscibility between the organic and aqueous phases, and extremely rapid reaction, the IP generally produces a defect-free ultrathin film on the organic side near the interface. The intrinsic characteristics of this polycondensation reaction are self-sealing and self-terminating due to the growing resistance of the self-cultured PA film because of polycondensation, thus, prohibiting any further diffusion of amine.[36] Compared to the conventional cellulose acetate-based asymmetric membranes, the TFC membranes have superior advantages such as higher water permeability, greater solute rejection, and nonbiodegradability. The high-water flux of TFC-FO membranes can be partially attributed to the high-hydrophilicity of aromatic PAs, which consist of the carboxylic acid structure due to the hydrolysis of the acyl chloride groups.[37–39]

The desired FO membranes should have characteristics of high-water permeability, low-solute permeability, and possess an ultrathin active layer supported by a relatively thin and fully porous hydrophilic substrate for minimizing the effect of internal concentration polarization (ICP). Because the IP reaction is fast and self-limiting, the resultant hydrophilic PA active layer is ultrathin, developing at the interface between two immiscible solutions of the organic and the aqueous phases. Although TFC membranes developed through IP are applicable to be used as FO membranes,[40] the fabrication schemes via IP to design RO and FO membranes may be quite different. The major differences between RO and FO membranes are their requirements for the membrane support. In the fabrication of RO membranes, one major consideration is the mechanical robustness of the porous support layer to withstand high-pressures of up to 60–100 bar, whereas FO is generally conducted under low or no pressures. As a result, the support layer for RO membranes is usually thick, hydrophobic and has a relatively low-porosity to withstand high-transmembrane pressures. The commercially available TFC RO membranes are fabricated through IP over a hydrophobic polysulfone (PSf) porous substrate supported by a nonwoven fabric. The thick hydrophobic support layer designed for RO may not be desirable for the FO application. When using conventional RO membranes in FO processes, a much lower water flux is obtained in the forward osmosis mode (referred as FO where the porous support layer is against the draw solution) compared to the pressure-retarded osmosis mode (referred as PRO where the dense active layer against the draw solution). This phenomenon is attributed to the occurrence of adverse ICP within the porous support layer. This ICP is different from the external concentration polarization (ECP) encountered in the pressure driven membrane processes.[41–46] It results in a sharp concentration gradient formed within the porous support layer. Moreover, the most serious fact is that the ICP within the membrane porous support cannot be eliminated by enhancing the cross-flow velocity and turbulence along the membrane surface. In addition, because FO membranes must contact two feed fluids simultaneously, which is different from RO processes (where only the active layer contacts the feed solution under pressure), the substrate physicochemical properties (hydrophilicity, porosity, pore size, pore-size distribution, and substructure resistance) play much more important roles on the resultant membrane performance. During the FO process, water transport through the semipermeable membrane is based on the solution-diffusion mechanism, while water and solutes in the feed and draw solutions diffuse within the porous support layer. Therefore, a highly porous support with enhanced hydrophilicity and thin thickness may facilitate the transport of water and solute and, thus, decrease ICP and membrane fouling.

In addition, the physicochemical properties of substrates play key factors in determining the formation, morphology, and performance of TFC-FO membranes. They affect the rate and the amount of phenylenediamine (PDA) diffusion to the reaction interface, thus, controlling the breadth of the reaction interface, the extent of IP reaction, and the PA layer thickness formed inside the pores. A hydrophilicity enhanced substrate may improve the binding between the PA layer and the substrate. However, hydrophilic substrates made from the addition of polyethylene glycol (PEG) and polyvinylpyrrolidone (PVP) into PSf appear to produce less permeable TFC RO membranes compared to hydrophobic PSf substrates, which is due to more PA formed inside the pores.[40] In addition, the water-soluble additives may swell and get washed away from the membrane matrix during long-time operations, which will influence the membrane stability. Introducing an amount of sulfonated polymer into the membrane matrix may adjust the hydrophilicity of the substrate and maintain the membrane long-term stability.

In this work, two kinds of membrane substrates, a commercial proprietary PVDF membrane and a lab-made polyethersulfone (PES)/sulfonated polysulfone (SPSf) porous membrane were used as the substrates for the fabrication of TFC-FO membranes via the IP reaction between *p*-phenylenediamine (PPDA) and trimesoyl chloride (TMC), as shown in Fig. 1. Seldom have studies been conducted on this monomer pair in TFC-FO membrane fabrication, and no one has used them for fabricating TFC-FO membranes. Different

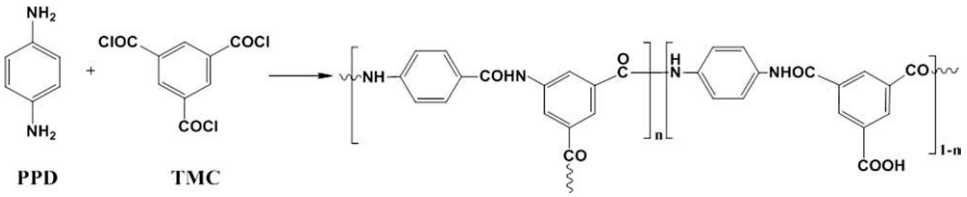

Figure 1. Scheme of IP reaction to form thin-film-composite PA membrane.

from previous approaches using low-molecular weight PEG and PVP,[40] a water insolvable but relatively hydrophilic SPSf was blended with PES to enhance the substrate wettability and long-term stability. For comparison, an asymmetric PES substrate was synthesized to fabricate PES TFC-FO membranes via the IP reaction under the same conditions. The effects of TFC-FO membrane structure on water and salt transports were investigated for water reuse and seawater desalination in FO processes. The transport intrinsic parameters of resultant TFC-FO membranes were determined through the hydraulic pressure-driven RO tests under low-pressures. It is believed that the fundamental study of membrane substrate and its effects on membrane formation and FO performance may elucidate important features of the IP reaction for the fabrication and optimization of TFC-FO membranes.

Experimental

Materials and PES/SPSf substrate fabrication

PPDA (>99%) and 1,3,5-benzenetricarbonyl trichloride (TMC, 98%) purchased from Sigma-Aldrich, were used as received. A commercial hydrophilic DURAPORE polyvinylidene fluoride (PVDF) filter with a pore size of 0.1 μm was used as the substrate (Millipore). The hydrophilic PVDF membrane was probably made by grafting hydroxyalkyl acrylate or methacrylate monomers upon a porous PVDF membrane so that the resultant membrane has a hydrophilic surface and inner pore walls.[47] PES [15.4% (w/v)] (Radel A, Solvay) and 2.2% (w/v) SPSf [lab-made with the ion-exchange capacities of 0.65 mEq g^{-1}] were dissolved in *N*-methyl-2-pyrrolidone (NMP, >99.5%, Merck, Germany) with 12.4 wt % diethylene glycol (DG, AR grade, Merck, Germany) to form the casting solution. The PES/SPSf-alloyed substrate was prepared by the Loeb-Sourirajan wet-phase inversion method. The casting solution was cast on a flat glass plate, followed by immersing it into a mixture of NMP/water (50/50 wt %) to form a porous substrate with a thickness of 60–100 μm. After being peeled off from the glass plate, the resultant membrane was rinsed with tap water for 6 h to remove the residual solvents. The selective top skin layer was formed during the phase inversion. An asymmetric PES substrate was synthesized from the dope of PES/NMP/DG 17.5/70.1/12.4 wt % according to the same procedure. Heptane (99%) and sodium chloride (NaCl, 99.5%) were purchased from Merck, Germany. The deionized (DI) water used in experiments was produced by a Milli-Q unit (Millipore) with a resistivity of 18 MΩ cm. PVP (Acros Organics, NJ) with different molecular weights was used to measure the pore size of membrane substrates through the solute transport method.

Formation of TFC polyamide membranes

The TFC-FO PA membranes were fabricated by first immersing the PVDF, PES, or PES/SPSf membrane substrates in an aqueous 2.0% (w/v) PPDA solution for 120 s. Note that only one side of substrates was in contact with the PPDA solution. After extracting from the solution, excess PPDA drops were removed from the support surface by tissue paper followed by blowing with air. Then a solution of 0.15% (w/v) TMC in heptane was poured on the surface of the PPDA-soaked membrane substrate for 30 s, which leads to the formation of an ultrathin PA film over the substrate. The resultant composite membrane was washed with ethanol to remove organic solvent residues and dried in air at 25°C for 30 min and then thoroughly washed with DI water to remove residual PPDA, and stored in DI water for further characterization. There was no thermal treatment or curing on the resultant composite membrane to prevent the membrane from dehydration, which may result in air bubbles trapped inside the membrane support layer.

Morphology and topology of substrates and TFC polyamide membranes

The membrane morphology was observed by a field emission scanning electronic microscope (FESEM, JEOL JSM-6700). The dry membrane samples (dried by a freeze dryer, ModulyoD, Thermo Electron Corporation) were fractured in liquid nitrogen. The membrane surface topology was examined using a Nanoscope IIIa atomic force microscope (AFM) from Digital Instruments. Small samples of the dried membranes (~0.5 cm^2) were glued on a metal substrate. For each membrane sample, an area of 2 × 2 μm^2 or 5 × 5 μm^2 was scanned at a rate of 1 Hz using the tapping mode. Various roughness parameters such as the mean roughness (R_a), root mean-square *Z* values (R_{ms}), and maximum vertical distance between the highest and lowest data points (R_{max}) were used to quantify the surface topology of membranes, which were determined from the averages of at least 10 sections of three samples.

Pore size and pore-size distribution of PES/SPSf membrane substrates

The pore size and pore-size distribution of PES and PES/SPSf membrane substrates were characterized by solute rejection experiments.[48,49] Generally, the solute rejections against PVPs with different molecular weights were tested under a hydraulic pressure of 5.0 bar. The solute diameter d_s is related to the molecular weight (M_W) as described in the following equation:

Table 1. Substrate Properties of PVDF Filter, PES, and PES/SPSf Substrates

Membrane Substrates	Water Permeability, A (L m^{-2} h^{-1} bar^{-1})	Mean Pore Size, d_p (nm)	MWCO (kDa)	Geometric Standard Deviation, σ_m	Porosity, ε_m	Contact angle, °
PVDF filter	2542.4	100*	–	–	0.895	Immediate wetting
PES substrate	411.4	12.8	211.6	1.65	0.815	78.5 ± 1.8
PES/SPSf substrate	505.2	15.9	150.2	1.16	0.833	73.5 ± 1.9

*From Millipore supplier.

$$d_s = 1.68 \times 10^{-2} \times M_w^{0.593} \quad (1)$$

When the solute rejection R_s is plotted *versus* d_s on log-normal probability paper, a straight line is yielded, and the mean effective pore size d_p in diameter is determined at $R_s = 50\%$, and the geometric standard deviation σ_p is found as the ratio of d_s at $R = 84.13\%$ and 50.0%. Then, the pore-size distribution of the membrane can be obtained. The comparison between different substrates was listed in Table 1.

Membrane porosity ε

To measure the membrane porosity, wet membranes were extracted from the water bath followed by careful and quick removal of excess water on the surface by tissue paper. The wet membranes were then weighed (m_1, g), freeze dried overnight, and reweighed (m_2, g). The water content is, thus, calculated as $m_1 - m_2$, and the dry weight of the membrane is m_2. As the densities of both water (ρ_w, 1.00 g cm^{-3}), PVDF (ρ_p, 1.77 g cm^{-3}) and PES (ρ_p, 1.37 g cm^{-3}) are known from suppliers, the overall porosity ε (%) of membrane is then obtained as follows:

$$\varepsilon = \frac{(m_1 - m_2)/\rho_w}{(m_1 - m_2)/\rho_w + m_2/\rho_p} \times 100 \quad (2)$$

Water contact angle of membrane substrates and TFC-FO membranes

For the evaluation of membrane hydrophilicity, contact angles of freeze-dried PES, PES/SPSf membrane substrates, and TFC-FO membranes were measured by a Contact Angle Geniometer (Rame Hart) using Milli-Q DI water as the probe liquid at 22 ± 0.5°C. To minimize the experimental error, the contact angle was randomly measured at six different locations for each sample, and the average was reported.

Mass transport characteristics of TFC-FO membranes

The water permeability and salt permeability of TFC-FO membranes were determined by testing the membranes under the RO mode. The filtration apparatus used is a stainless steel dead-end stirred cell resting on a magnetic stir plate. The feed chamber was pressurized by nitrogen gas. The filtration cell has a capacity of 0.350 L and effective membrane area of 19.5 cm^2. All tests are conducted at room-temperature (25°C). The water permeability coefficient (A) was obtained from the pure water permeation flux under the applied transmembrane pressures of 0 ∼ 5.0 bar. The salt rejection (R_s) was determined using a feed water containing 1000 ppm NaCl based on conductivity measurements of the permeate and feed. The salt permeability coefficient (B), which is the intrinsic property of a membrane to retain salt, was determined based on the solution-diffusion theory:[11,50,51]

$$\frac{1 - R_s}{R_s} = \frac{B}{A(\Delta P - \Delta\pi)} \quad (3)$$

where ΔP and $\Delta\pi$ are the pressure difference and osmotic pressure difference across the membrane, respectively.

Water flux through forward osmosis tests

FO experiments were conducted on a lab-scale crossflow filtration unit, as shown in Fig. 2. The crossflow permeation cell was a plate-and-frame design with a rectangular channel (8.0 cm in length, 2.0 cm in width, and 0.28 cm in height) on each side of the membrane. There is no spacer in the flow channels. The flow velocities of solutions during the FO testing were kept at 0.26 L min^{-1} (corresponding to a linear velocity of 8.3 cm s^{-1}) for both the feed and draw solutions, which flowed cocurrently along the membrane. The temperatures of the feed and draw solutions were

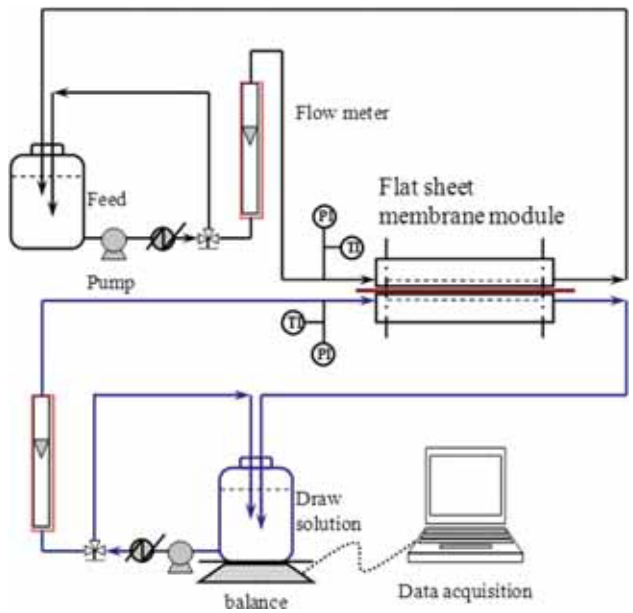

Figure 2. Schematic diagram of the lab-scale FO set-up (co-current flowing of feed and draw solutions).

[Color Figure can be viewed in the online issue, which is available at wileyonlinelibrary.com.]

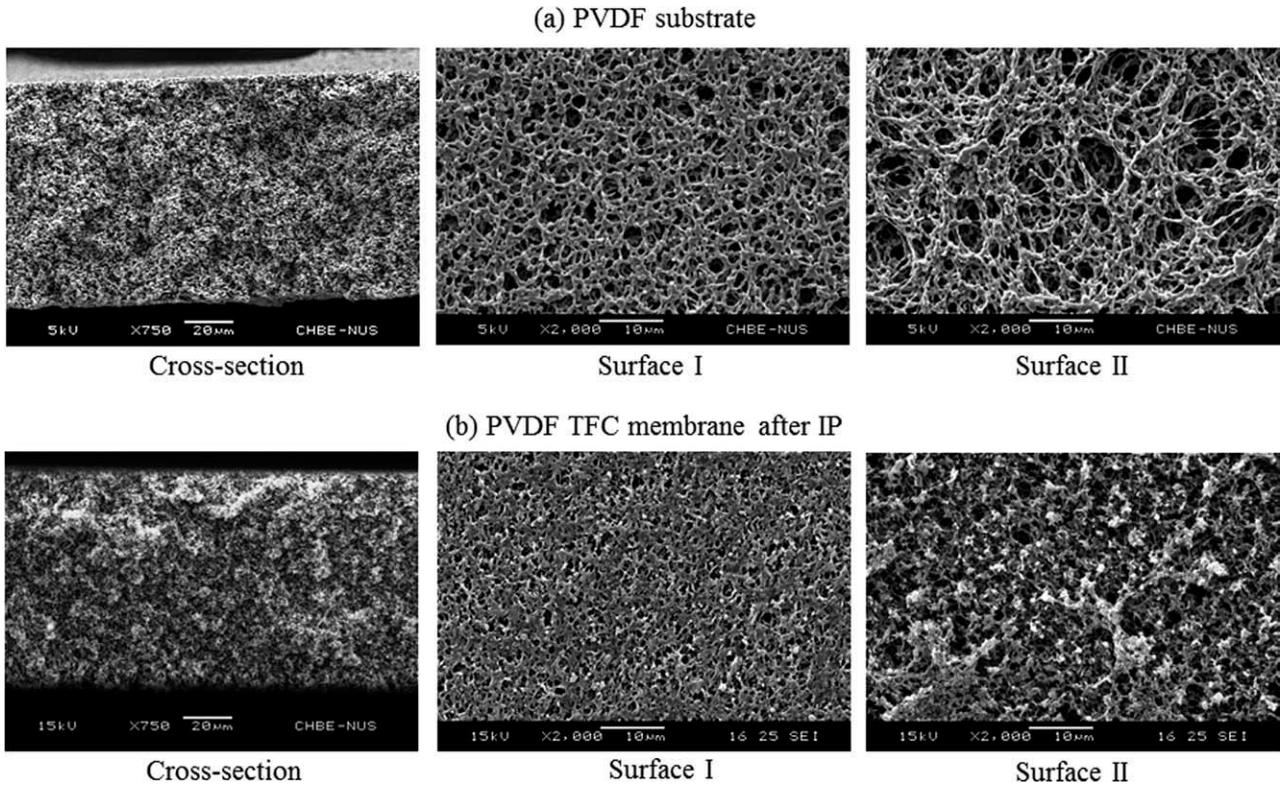

Figure 3. Morphology of (a) PVDF substrate and (b) PVDF TFC-FO membrane via IP.

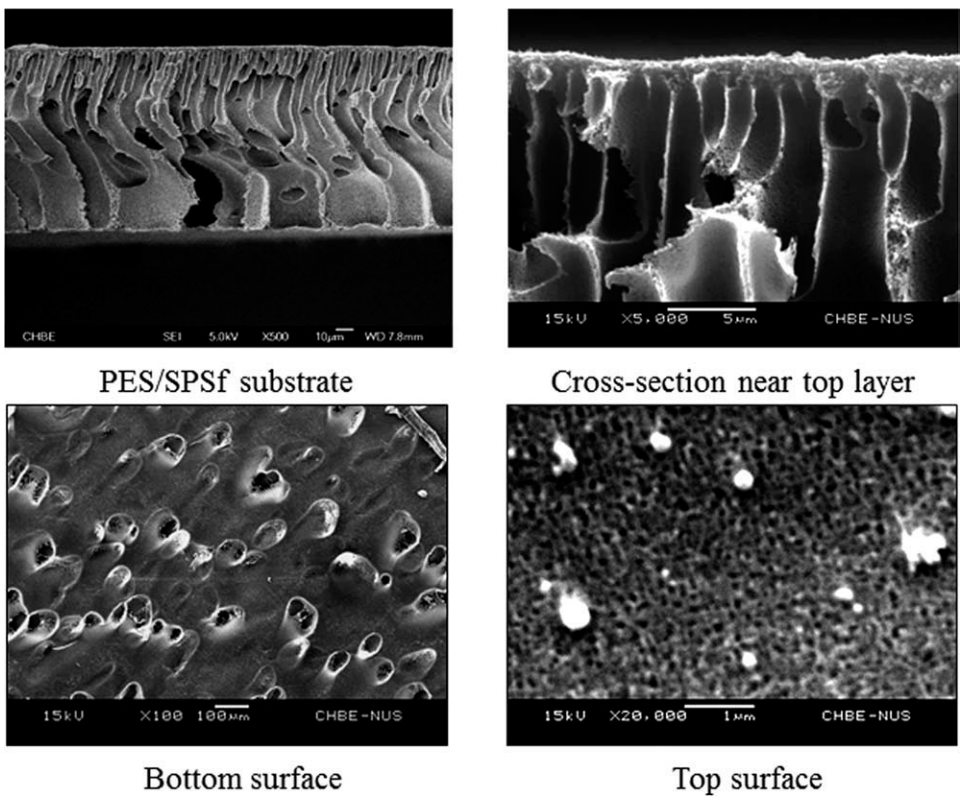

Figure 4. Morphology of the PES/SPSf-alloyed membrane substrate.

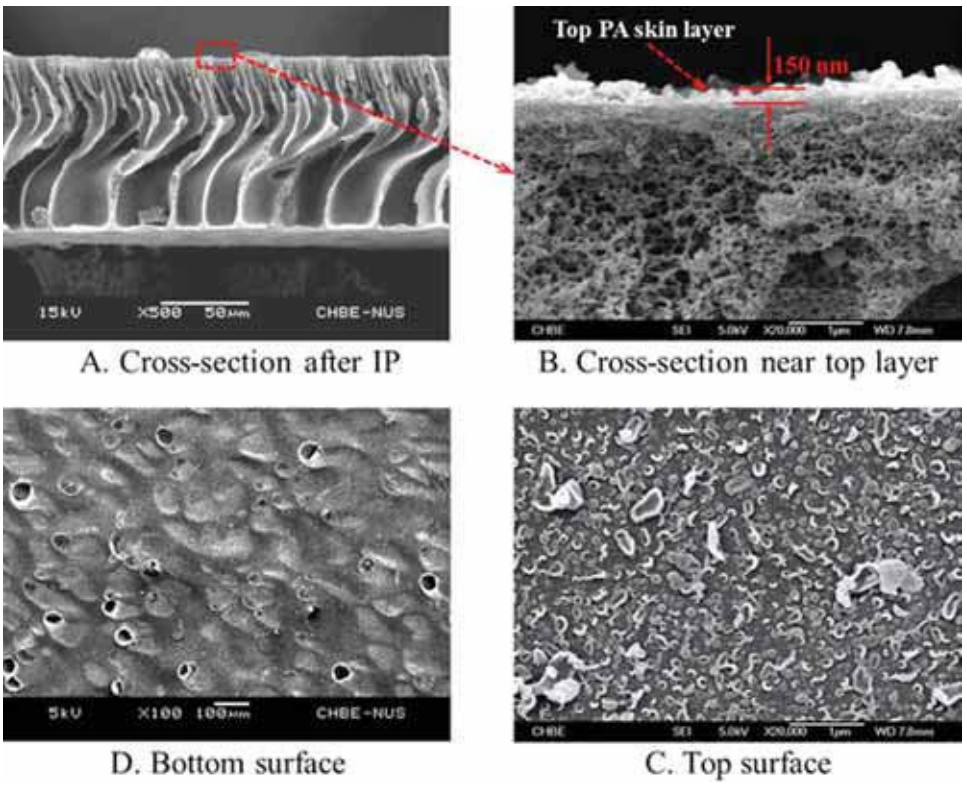

Figure 5. Morphology of the PES/SPSf TFC-FO membrane.

[Color figure can be viewed in the online issue, which is available at wileyonlinelibrary.com.]

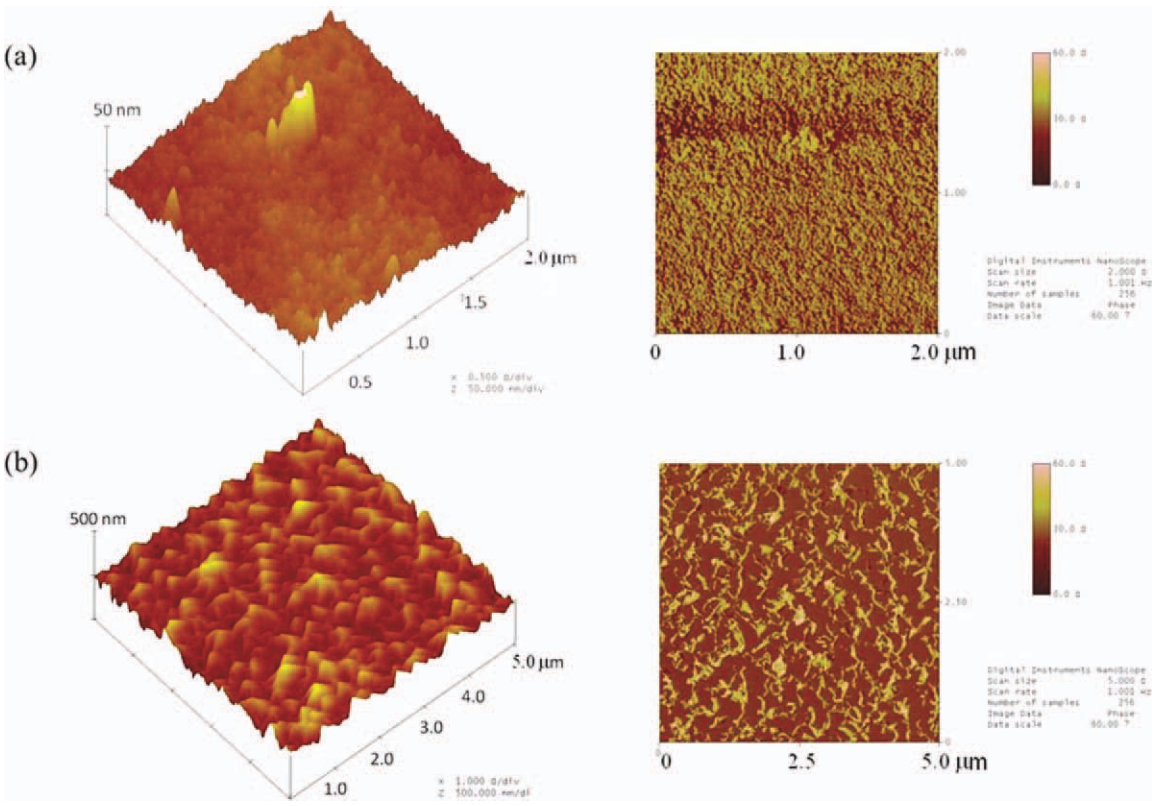

Figure 6. AFM of (a) PES/SPSf substrate and (b) PES/SPSf TFC-FO membrane.

[Color figure can be viewed in the online issue, which is available at wileyonlinelibrary.com.]

Table 2. Surface Roughness of PES/SPSF Substrate and PES/SPSf TFC-FO Membrane

Membranes	R_a (nm)	R_{ms} (nm)	R_{max} (nm)
PES/SPSf substrate	5.19 (±0.45)	7.04 (±0.56)	71.2 (±7.8)
PES/SPSf TFC-FO	44.1 (±3.9)	54.4 (±4.7)	366.2 (±23.5)

Note: R_a, mean roughness; R_{ms}, root mean square of Z values; R_{max}, maximum vertical distance between the highest and lowest data points. The values in the brackets are standard deviation.

maintained at 22 ± 0.5°C. NaCl solutions with different concentrations were prepared and used as the draw solutions. DI water and concentrated NaCl solutions were used as the feed solutions.

During FO tests, the dilution of the draw solution was ignored, because the ratio of water permeation flux to the volume of the draw solution was less than 2%. The membranes were tested in two different operation modes. In the PRO mode, the membrane selective layer formed during the IP reaction was against the draw solution while in the FO mode, the draw solution was in contact with the porous support layer. Each experiment was conducted for 30 min and repeated three times.

The water permeation flux (J_w, L m^{-2} h^{-1}, abbreviated as LMH) is calculated from the volume change of the feed or draw solution,

$$J_w = \frac{\Delta V}{S_m \Delta t} \tag{4}$$

where ΔV (L) is the volume of water that has permeated across the membrane in a predetermined time Δt (h) during the FO process and S_m is the effective membrane surface area (m^2).

When DI water was used as the feed, the reverse salt flux (i.e., salt reverse diffusion) from the draw solution to the feed was calculated by measuring the salt concentration in the feed solution at the end of each experiment. The salt concentration in the feed was determined by conductivity measurement based on a calibration curve for the salt solution. Then, the reverse salt flux, J_s in g m^{-2} h^{-1} (abbreviated as gMH), can be obtained by considering the increase in the feed salt content as follows:

$$J_s = \frac{\Delta(C_t V_t)}{S_m \Delta t} \tag{5}$$

where C_t and V_t are the salt concentration and the volume of the feed at the end of FO tests, respectively.

The water flux in FO processes can be modeled by the following equations.[11,41] For PRO mode (selective layer against the draw solution):

$$J_w = \frac{1}{K_m} \ln \frac{A\pi_{D,m} - J_w + B}{A\pi_{F,b} + B} \tag{6}$$

For FO mode (selective layer against the feed):

$$J_w = \frac{1}{K_m} \ln \frac{A\pi_{D,b} + B}{A\pi_{F,m} + J_w + B} \tag{7}$$

where $\pi_{D,b}$ and $\pi_{F,b}$ refer to the osmotic pressures in the respective bulk draw solution and feed, $\pi_{D,m}$ and $\pi_{F,m}$ are the corresponding osmotic pressures on membrane surfaces in the draw and feed solutions after considering the ECP effect,[45,46] and K_m is the solute resistivity for diffusion within the porous layer given by Eq. 8, involving salt diffusivity D_s, membrane structural parameter S, membrane turtuosity τ, membrane thickness l, and membrane porosity ε:

$$K_m = \frac{S}{D_s} = \frac{l\tau}{\varepsilon D_s} \tag{8}$$

Results and Discussion

Morphology and topology of membrane substrates and TFC-FO membranes

From Fig. 3, the hydrophilic PVDF substrate has an almost symmetric structure although the pore size on the top surface is smaller than that on the bottom surface. The

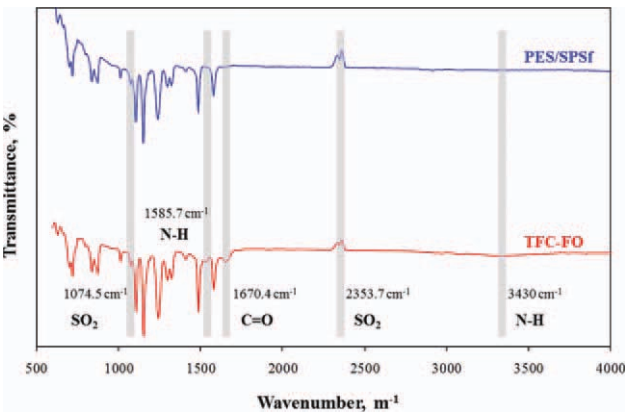

Figure 7. FTIR spectra of PES/SPSf substrate and TFC-FO membranes.

[Color figure can be viewed in the online issue, which is available at wileyonlinelibrary.com.]

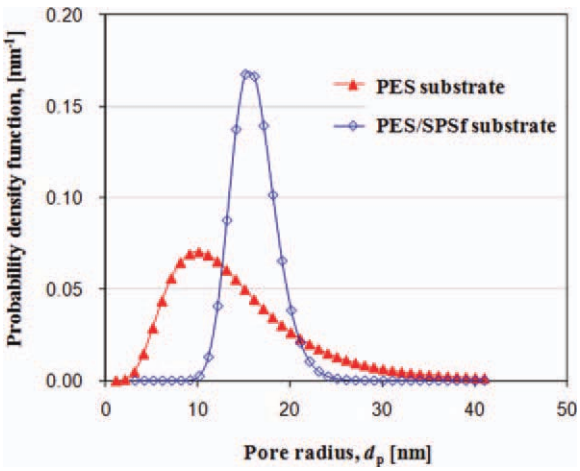

Figure 8. Pore-size distribution of PES and PES/SPSf membrane substrates.

[Color figure can be viewed in the online issue, which is available at wileyonlinelibrary.com.]

Table 3. Transport Properties and Structure Parameters of PVDF-TFC and PES/SPSf -TFC FO Membranes

Membranes	Water Permeability, A [L m^{-2} h^{-1} bar^{-1} (m s^{-1} Pa^{-1})]	Salt Permeability*, B [L m^{-2} h^{-1} (m s^{-1})]	K_m** (s m^{-1})	S** (m)
PVDF TFC	0.82 (2.28×10^{-12})	0.19 (5.28×10^{-8})	2.27×10^{5}	3.29×10^{-4}
PES/SPSf TFC	0.77 (2.14×10^{-12})	0.11 (3.05×10^{-8})	1.86×10^{5}	2.38×10^{-4}

*1000 ppm NaCl as the feed solution in the RO test.
**2.0 M NaCl as the draw solution and DI water as feed in the FO mode.

overall porosity of this PVDF substrate is about 0.895, which produces a very high pure water permeability of 2542.4 LMH bar^{-1}. After the IP reaction between PPDA and TMC on the top surface, it is found that the top surface (contacting with the aqueous PPDA solution) is not fully covered by the PA layer although the surface becomes smoother. This may be attributed to the fact that the pore on the top surface is very big, which induces the IP reaction to take place inside the membrane matrix. Because of the high-hydrophilicity of this PVDF substrate, the aqueous PPDA solution may penetrate into the whole membrane and the IP reaction may even happen on the bottom layer, which can be verified by the decreased porosity in the bottom layer from scanning electronic microscopy images.

Fig. 4 shows the morphology of the lab-made PES/SPSf substrate. It has an asymmetric membrane structure consisting of a thin sponge-like top layer (1.2 ± 0.1 μm in thickness), a porous middle layer full of finger-like macrovoids (93.5 ± 7.5 μm in thickness) and a thin bottom layer ($\sim$1.0 μm in thickness). This structure is formed due to the use of a mixed solvent/nonsolvent coagulant system that facilitates the formation of a thin skin layer having uniform pores and higher porosity. Very big pores interconnecting with finger-like macrovoids are observed on the bottom surface that may mitigate ICP effects within the porous substrate. Fig. 5 illustrates the top surface and cross-section morphology after IP reaction. A thin active PA layer with an average thickness of 150 nm is formed in a ridge-and-valley morphology. This is the functional dense-selective layer for separation. The bottom surface exhibits little change of morphology, which verifies less IP reaction happening.

From the two- and three-dimensional AFM images in Fig. 6, it can be observed that the surface roughness has a sharp increase after the IP reaction on the top surface of the PES/SPSf substrate. The surface roughness parameters which are expressed in terms of the mean roughness (R_a), the root mean square of the Z value (R_{ms}) and the mean difference between the highest peaks and lowest valleys (R_{max}) are given in Table 2. The mean-square surface roughness (R_{ms}) changes from 7.04 to 54.4 nm.

Characterization of PES, PES/SPSf substrates and TFC-FO membranes

Fig. 7 shows FTIR spectra of the PES/SPSf-alloyed membrane and the PES/SPSf TFC-FO membrane. It is noted that the characteristic peaks of the symmetric stretching vibration at 2353.7 cm^{-1} and the asymmetric stretching vibration at 1074.5 cm^{-1} appear for the sulfonic acid group. The wide peak at 3400–3500 cm^{-1} indicates the stretching vibration of the hydrogenation N—H band of TFC-FO membranes. Peaks at 1585.7 cm^{-1} are the stretching vibration of carbonyl (N—H, amide II peak). Peaks at 1670.4 cm^{-1} indicate the stretching vibration of carbonyl (C=O, amide I peak).[52] The PA —CO—NH— structure formed from an IP reaction between PDA and TMC has a crosslinked portion and linear moiety (Fig. 1). The crosslinked PA portion has free carboxylic acid groups from the hydrolysis of unreacted acid chloride groups, which can enhance the hydrophilicity of TFC-FO membranes and improve water permeability.[36,37,53] The performance and efficiency of the FO membrane primarily depend on the nature of the selective layer composed of the partially cross-linked aromatic PA.

Blending SPSf into the PES substrate has several effects. It enhances the substrate hydrophilicity by lowering the contact angle of PES from 78.6° to 73.5° with the addition of 2.2 wt % SPSf into the PES/SPSf-alloyed substrate. The hydrophilic SPSf can alter the phase inversion path, modify the substrate structure, and result in a thin dense top layer and a porous support layer. The overall porosity of this PES/SPSf substrate is about 0.833. The PES/SPSf substrate has a pure water permeability of 505.2 LMH bar^{-1} and a mean pore size in diameter of 15.9 nm, which is consistent with FESEM images of the top surface as shown in Fig. 4. Its molecular weight cut-off is about 150.2 kDa. Compared with the hydrophilic PVDF substrate, the PES/SPSf substrate has a smaller pore size and surface porosity, subsequently lower water permeability. The fabricated asymmetric PES substrate has a smaller mean pore size of 12.8 nm in diameter but a wide pore-size distribution, as shown Fig. 8. As a result, the PES substrate has a lower water permeability of 411.4 LMH bar^{-1}.

Water permeability coefficient and salt permeability coefficient

Table 3 summarizes the membrane separation properties, i.e., water permeability coefficient A and salt permeability coefficient B, of these TFC-FO membranes under pressure. The pure water permeability of the PVDF TFC-FO membrane is slightly higher than that of the PES/SPSf TFC-FO

Table 4. Salt Rejections of PES/SPSf TFC Membranes Under Pressures

Salt*	Salt Rejection (%)	Pressure (bar)
NaCl	93.5	5.0
NaCl	96.5	10.0
$MgCl_2$	96.6	5.0
$MgSO_4$	97.8	5.0

*1000 ppm salt as the feed solution in the RO test.

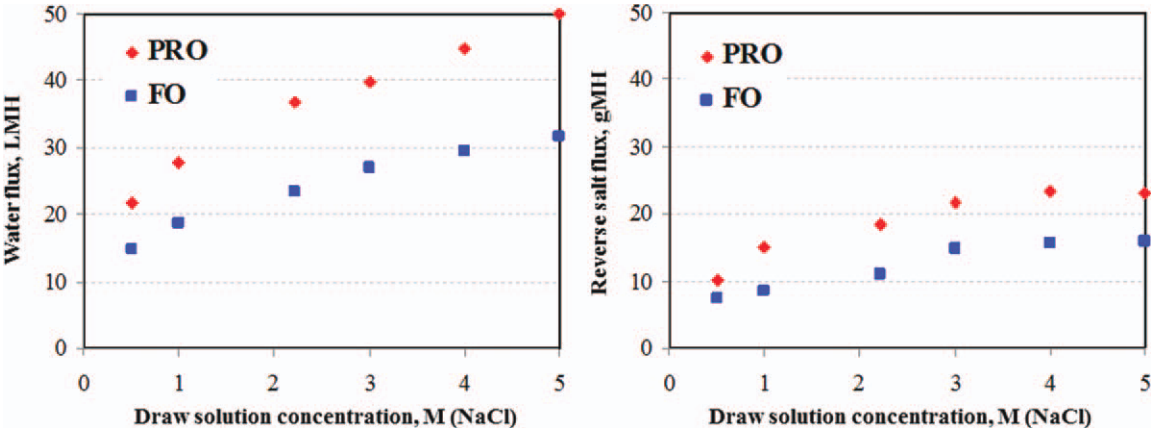

Figure 9. Water permeation flux and reverse salt flux through PVDF TFC membrane against NaCl concentration in draw solution.

Experimental conditions; crossflow velocity and temperature of both feed and draw solutions of 8.3 cm s^{-1} and 22 ± 0.5 °C, respectively. [Color figure can be viewed in the online issue, which is available at wileyonlinelibrary.com.]

membrane (i.e., 0.82 *vs.* 0.77 LMH bar^{-1}), but the former has a higher NaCl salt permeability than the latter (0.19 *vs.* 0.11 LMH). In addition, the TFC membrane shows higher rejections against divalent ions ($MgCl_2$, $MgSO_4$) and lower rejection against monovalent ions (NaCl), as listed in Table 4. The salt rejection increases with an increase in transmembrane pressure. The structural parameters of PES/SPSf and TFC-FO membranes are determined by fitting the experimental data of Figs. 9 and 10 into Eq. 7, respectively, and their values are lower than reported data,[26,27] indicating a lower ICP effect in the support layer.

Water flux through the TFC-FO membranes

Fig. 9 shows the water fluxes of TFC-FO membranes derived from the PVDF substrate using concentrated NaCl solutions as draw solutions and DI water as the feed solution. The water flux increases with an increase in draw solution concentration because a larger effective osmotic pressure provides a greater driving force. Water fluxes of 50.0 LMH and 32.4 LMH for PRO and FO modes, respectively, are achieved under 5.0 M NaCl as the draw solution. The water flux in the PRO mode is much higher than that in the FO mode, which is attributed to the serious ICP within the porous layer. However, the water flux *versus* salt concentration deviates from linearity due to the decreased effective driving force, especially at higher salt concentrations. The reduction in the effective driving force may be resulted from two factors, i.e., severer dilutive ECP within the boundary layer at the membrane surface and ICP within the support layer due to the salt leakage from the draw solution to the feed. The reverse salt fluxes observed under PRO and FO modes also increase with increasing draw solution concentration, and reach 23.2 and 16.7 gMH, respectively, under 5.0 M NaCl as the draw solution.

Fig. 10 shows the water flux of the TFC-FO membrane derived from the PES/SPSf substrate. The water flux exhibits the same trend as the PVDF TFC-FO membrane but with a

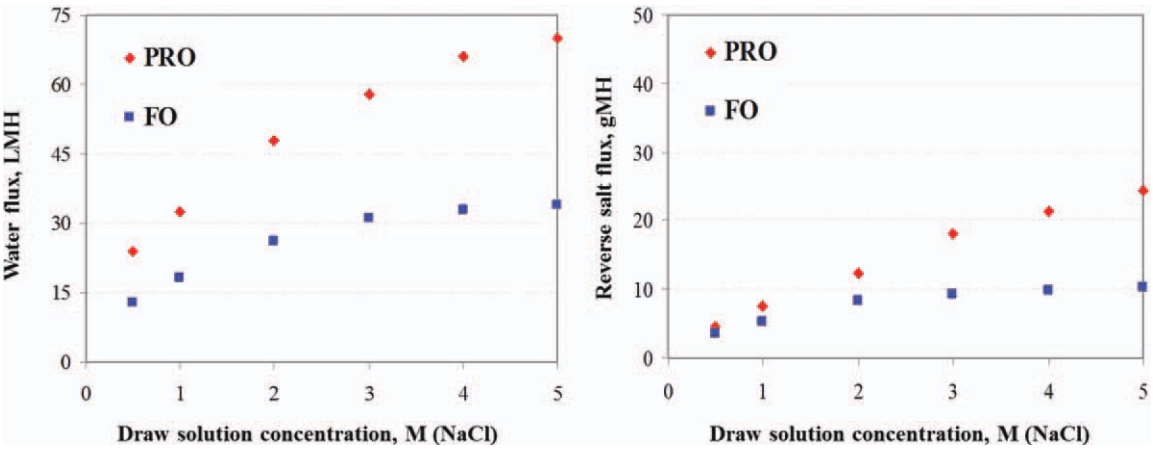

Figure 10. Water permeation flux and reverse salt flux through PES/SPSf TFC-FO membrane against NaCl concentration in draw solution.

Experimental conditions: Feed: DI water; crossflow velocity and temperature of both feed and draw solutions of 8.3 cm s^{-1} and 22 ± 0.5 °C, respectively. [Color figure can be viewed in the online issue, which is available at wileyonlinelibrary.com.]

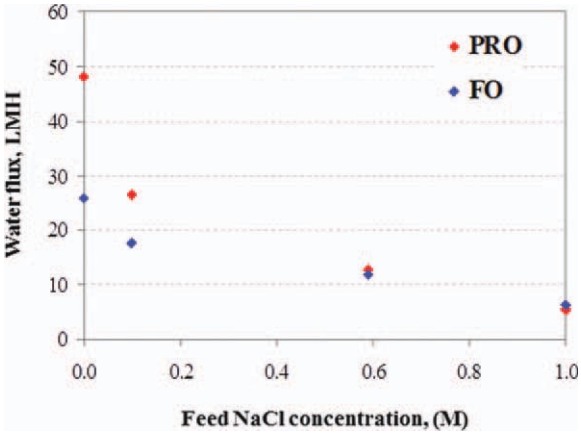

Figure 11. Effect of feed NaCl concentration on water permeation flux through the PES/SPSf TFC-FO membrane.

Experimental conditions: draw solution: 2.0 M NaCl; crossflow velocity and temperature of both feed and draw solutions of 8.3 cm s^{-1} and 22 ± 0.5 °C. [Color figure can be viewed in the online issue, which is available at wileyonlinelibrary.com.]

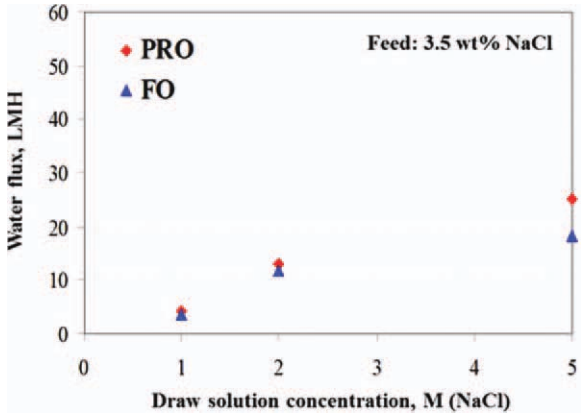

Figure 12. Water permeation flux against NaCl concentration in draw solution.

Experimental conditions: Feed: 3.5 wt % NaCl; crossflow velocity and temperature of both feed and draw solutions of 8.3 cm s^{-1} and 22 ± 0.5 °C, respectively. [Color figure can be viewed in the online issue, which is available at wileyonlinelibrary.com.]

much higher water permeability and lower salt permeability. Water fluxes of 47.5 and 69.8 LMH are achieved under the PRO mode using 2.0 and 5.0 M NaCl as the draw solution, respectively. In addition, the water flux difference between PRO and FO modes become larger compared to that of the PVDF TFC-FO membrane. This may be attributed to the totally different substrate structures. The PVDF substrate has an almost symmetric structure but the PES/SPSF substrate has an asymmetric structure. Moreover, because the selective layer of the PVDF TFC-FO membrane is located underneath the surface as indicated in Fig. 4, the extra ICP occurs in the porous surface layer above the selective layer of the PVDF TFC-FO membrane at the draw solution side. On the other hand, the selective layer of the PES/SPSf TFC-FO membrane is located on the top surface, which can mitigate the ICP effect in the PRO mode although cannot eliminate the ICP effect due to the salt leakage. As a result, PVDF TFC membrane has a higher Km value than PES/SPSf TFC membrane. In the FO mode, the water flux levels off after NaCl draw solution increases to 2.5 M. The ICP within the porous bottom layer is the main reason for the less increase in water flux at higher concentrations of draw solution. The reverse salt flux in the FO mode is much less than that in the PRO mode and shows no increment after 2.5 M NaCl as the draw solution due to the increased salt diffusion resistance within the porous support layer. The water flux of PES/SPSf TFC-FO membrane is over three orders of magnitude higher than the reverse salt flux for the corresponding draw solution used in the FO process.

The TFC-FO membrane fabricated from the control PES substrate has lower water fluxes of 32.8 and 21.3 LMH, but higher salt leakages of 44.7 and 36.5 gMH in the PRO and FO modes, respectively, under 2.0 M NaCl as the draw solution. The higher salt leakages may be due to the wide pore-size distribution of the PES substrate where larger pores cannot be completely covered by the PA layer. In addition, nonuniform dispersion of PPDA solution on the less hydrophilic PES substrate surface with a wide pore-size distribution and many larger pores may be another reason to produce defects on the subsequent TFC-FO membrane.

Table 5. Comparison of FO Membrane Performance

Membranes	Water Flux (PRO/FO) (L m^{-2} h^{-1})	Reverse Salt Flux (PRO/FO) (g m^{-2} h^{-1})	Draw Solution	Feed	References
PES/SPSf TFC FO	24.1/13.0	4.5/3.6	0.5 M NaCl	DI water	This work
PES/SPSf TFC FO	47.5/26.0	12.4/8.3	2.0 M NaCl	DI water	This work
PES/SPSf TFC FO	12.7/11.8	–	2.0 M NaCl	3.5 wt % NaCl	This work
#B-FO hollow fiber	32.2/13.5	3.5/1.8	0.5 M NaCl	DI water	26
#B-FO hollow fiber	46.0/22.5	4.4/2.5	2.0 M NaCl	DI water	26
TFC FO flat sheet	18.0 (FO)	–	1.5 M NaCl	DI water	27
#C-FO hollow fiber	42.6/18.5	4.0/1.5	0.5 M NaCl	DI water	28
#C-FO hollow fiber	68.0/29.5	5.8/2.6	2.0 M NaCl	DI water	28
#C-FO hollow fiber	12.4/12.4	–	2.0 M NaCl	3.5 wt % NaCl	28
HTI flat sheet membrane	18.6 (PRO)	–	0.5 M NaCl	DI water	43
HTI flat sheet membrane	13.0 (FO)	10.5	2.0 M NaCl	DI water	54
HTI flat sheet membrane	11.2 (PRO)	–	2.0 M NaCl	3.5 wt % NaCl	44

*Forward osmosis experiment conducted at 20–25°C. PRO/FO in bracket: pressure-retarded osmosis mode/forward osmosis mode.

Water flux against concentrated NaCl solutions as the feed

Fig. 11 shows that the water flux decreases when replacing DI water by concentrated NaCl solutions as the feed. Interestingly, the water flux difference between PRO and FO modes becomes less gradually with an increase in feed concentration. This demonstrates that the ICP within the porous substrate layer in the feed or draw solution side becomes the main resistance to water transport.[54] When using the model 3.5 wt % NaCl solution as the feed, Fig. 12 shows the water transport performance as a function of NaCl concentration in draw solutions under different membrane orientations. Water fluxes of 12.7 LMH (PRO mode) and 11.8 LMH (FO mode) are obtained under 2.0 M NaCl as the draw solution, which is similar to the reported TFC-FO membranes as listed in Table 5. The water flux difference between PRO and FO modes during seawater desalination is reduced compared to that when DI water is used as the feed solution. This is due to the reduction in overall osmotic pressure difference because of the use of 3.5 wt % NaCl as the feed solution. Moreover, because the concentration polarization, whether internal or external, is a function of water permeation flux and effective mass-transfer coefficient, the reduced water flux will mitigate the concentration polarization, which reduces the difference between PRO and FO modes under the same draw solution.

Conclusions

We have developed high-flux TFC-FO membranes with the aid of IP on a porous polymeric support with enhanced hydrophilicity and tailored structure. PPDA and 1,3,5-trimesoylchloride are the monomers for the thin-film polycondensation reaction to form a thin aromatic PA selective layer on the substrate. Two kinds of substrates, a commercial proprietary PVDF support with the nominal pore diameter of 100 nm and a lab-made PES/SPSf-alloyed porous membrane with a mean pore size of 15.9 nm in diameter, are used to investigate the effect of substrate structure on the performance of TFC-FO membranes. It is found that the IP reaction cannot cover larger surface pores, which may result in a lower water flux due to the ICP effect within the porous layer. The formation of TFC-FO membrane on the hydrophilicly modified PES/SPSf substrate exhibits a high-water flux in the FO process. It has a water flux of 69.8 LMH under 5.0 M NaCl as the draw solution and DI water as the feed in the PRO mode. The water flux decreases to 25.2 LMH in seawater desalination (i.e., 3.5 wt % NaCl solution) under the same draw solution concentration. The TFC-FO PA membrane can be fabricated on the PES/SPSf membrane without post-treatments using thermal annealing to spare extra cost and complicity. Further improving the substrate substructure and IP reaction parameters may enhance the water permeability and reduce the ICP effect within the porous layer.

Acknowledgments

The authors thank financial support from King Abdullah University of Science and Technology (KAUST) by Award No SA-C0005/UK-C0002, and National University of Singapore (NUS) for funding this research project with the grant number of and R-279-000-265-598. Special thanks are due to Dr. Youchang Xiao, Dr. Jincai Su, Mr. Shipeng Sun, and Ms. Rui Chin Ong for their valuable suggestions.

Nomenclature

A = water permeability, L m^{-2} h^{-1} bar^{-1}
B = salt permeability, L m^{-2} h^{-1}
C_t = salt concentration, mol L^{-1}
d_p = pore diameter, nm
d_s = solute diameter, nm
D_s = diffusion coefficient of salt in the membrane substrate, m^2 s^{-1}
ECP = external concentration polarization
FO = forward osmosis
ICP = internal concentration polarization
IP = interfacial polymerization
J_s = reverse salt flux, g m^{-2} h^{-1}
J_w = water flux, L m^{-2} h^{-1}
k = water transport coefficient, m s^{-1}
k_b = mass-transfer coefficient, m s^{-1}
k_D = mass-transfer coefficient, m s^{-1}
K_m = solute diffusion resistivity within the porous layer, s m^{-1}
l = thickness, m
m = membrane weight, g
MWCO = molecular weight cut-off, kDa
P = pressure, bar
PRO = pressure-retarded osmosis
R = solute rejection
S = membrane structural parameter, m
S_m = effective membrane surface area, m^2
TFC = thin-film-composite
Δt = operation time interval, h
ΔV = water permeation volume, L
V_t = volume of the feed at a time interval of Δt, L
ε = porosity
π = osmotic pressure, bar
ρ = material density, g cm^{-3}
σ = geometric standard deviation
τ = turtuosity

Subscripts

b = bulk solution
D = draw solution side
F = feed solution side
i = inside of the active layer within the porous support
m = membrane
s = solute

Literature Cited

1. Semiat R. Energy issues in desalination processes. *Environ Sci Tech.* 2008;42:8193–8201.
2. Shannon MA, Bohn PW, Elimelech M, Georgiadis JG, Marias BJ, Mayes AM. Science and technology for water purification in the coming decades. *Nature*. 2008;452:301–310.
3. Cath TY, Childress AE, Elimelech M. Forward osmosis: principles, applications, and recent developments. *J Membr Sci*. 2006;281:70–87.
4. Cornelissen ER, Harmsen D, Korte KFD, Ruiken CJ, Qin JJ, Oo H, Wessels LP. Membrane fouling and process performance of forward osmosis membranes on activated sludge. *J Membr Sci*. 2008; 319:158–168.
5. Kessler JO, Moody CD. Drinking water from sea water by forward osmosis. *Desalination*. 1976;18:297–306.
6. McCutcheon JR, McGinnis RL, Elimelech M. A novel ammonia-carbon dioxide forward (direct) osmosis desalination process. *Desalination*. 2005;174:1–11.
7. McGinnis RL, Elimelech M. Global challenges in energy and water supply: the promise of engineered osmosis. *Environ Sci Technol.* 2008;42:8625–8629.
8. Miller JE, Evans LR. *Forward Osmosis: A New Approach to Water Purification and Desalination*. Albuquerque, NM: Sandia National Laboratories Report, 2006.

9. Jiao B, Cassano A, Drioli E. Recent advances on membrane processes for the concentration of fruit juices: a review. *J Food Eng*. 2004;63:303–324.
10. Holloway RW, Childress AE, Dennett KE, Cath TY. Forward osmosis for concentration of anaerobic digester centrate. *Water Res*. 2007;41:4005–4014.
11. Lee K, Baker R, Lonsdale H. Membranes for power generation by pressure-retarded osmosis. *J Membr Sci*. 1981;8:141–171.
12. Loeb S. One hundred and thirty benign and renewable megawatts from Great Salt Lake? The possibilities of hydroelectric power by pressure retarded osmosis. *Desalination*. 2001;141:85–91.
13. McGinnis RL, McCutcheon JR, Elimelech M. A novel ammonia-carbon dioxide osmotic heat engine for power generation. *J Membr Sci*. 2007;305:13–19.
14. Yang Q, Wang KY, Chung TS. A novel dual-layer forward osmosis membrane for protein enrichment and concentration. *Sep Purif Technol*. 2009;69:269–274.
15. Elimelech M. Yale constructs forward osmosis desalination pilot plant. *Membr Technol*. 2007;1:7–8.
16. Mi B, Elimelech M. Chemical and physical aspects of organic fouling of forward osmosis membranes. *J Membr Sci*. 2008;320:292–302.
17. Mi B, Elimelech M. Gypsum scaling and cleaning in forward osmosis: measurement and mechanisms. *Environ Sci Technol*. 2010; 44:2022–2028.
18. Mi B, Elimelech M. Organic fouling of forward osmosis membranes: fouling reversibility and cleaning without chemical reagents. *J Membr Sci*. 2010:348:337–345.
19. Lee S, Boo C, Elimelech M, Hong S. Comparison of fouling behavior in forward osmosis (FO) and reverse osmosis (RO). *J Membr Sci*. 2010;365:34–39.
20. Herron J. *Asymmetric forward osmosis membranes*. US Patent 7445712, Hydration Technologies Inc., Albany, OR, US (2005).
21. Wang KY, Chung TS, Qin JJ. Polybenzimidazole (PBI) nanofiltration hollow fiber membranes applied in forward osmosis process. *J Membr Sci*. 2007;300:6–12.
22. Yang Q, Wang KY, Chung TS. Dual-layer hollow fibers with enhanced flux as novel forward osmosis membranes for water production. *Environ Sci Technol*. 2009;43:2800–2805.
23. Su J, Yang Q, Teo JF, Chung TS. Cellulose acetate nanofiltration hollow fiber membranes for forward osmosis processes. *J Membr Sci*. 2010;355:36–44.
24. Wang KY, Ong RC, Chung TS. Double-Skinned forward osmosis membranes for reducing internal concentration polarization within the porous sublayer. *Ind Eng Chem Res*. 2010;49:4824–4831.
25. Zhang S, Wang KY, Chung TS, Chen HM, Jean YC, Amy G. Well-constructed cellulose acetate membranes for forward osmosis: minimized internal concentration polarization with an ultra-thin selective layer. *J Membr Sci*. 2010;360:522–535.
26. Wang R, Shi L, Tang CY, Chou S, Qiu C, Fane AG. Characterization of novel forward osmosis hollow fiber membranes. *J Membr Sci*. 2010;355:158–167.
27. Yip NY, Tiraferri A, Phillip WA, Schiffman JD, Elimelech M. High performance thin-film composite forward osmosis membrane. *Environ Sci Technol*. 2010;44:3812–3818.
28. Chou S, Shi L, Wang R, Tang CY, Qiu C, Fane AG, Characteristics and potential applications of a novel forward osmosis hollow fiber membrane. *Desalination*. 2010;261:365–372.
29. Rozelle LT, Cadotte JE, Cobian KE, Kopp CV Jr. *Nonpolysaccharide membranes for reverse osmosis: NS-100 membranes*. In: Sourirajan S, editor. *Reverse Osmosis and Synthetic Membranes*, Ottawa: National Research Council of Canada, 1977, *Chapter 12*.
30. Cadotte JE. *Interfacially synthesized reverse osmosis membrane*. US Patent 4,277,344, FilmTec Corp., MN US (1981).
31. Petersen RJ. Composite reverse-osmosis and nanofiltration membranes. *J Membr Sci*. 1993;83:81–150.
32. Veríssimo S, Peinemann K-V, Bordado J. Thin-film composite hollow fiber membranes: an optimized manufacturing method. *J Membr Sci*. 2005;264:48–55.
33. Ghosh AK, Jeong BH, Huang XF, Hoek EMV. Impacts of reaction and curing conditions on polyamide composite reverse osmosis membrane properties. *J Membr Sci*. 2008;311:34–45.
34. Abu Tarboush BJ, Rana D, Matsuura T, Arafat HA, Narbaitz RM. Preparation of thin-film-composite polyamide membranes for desalination using novel hydrophilic surface modifying macromolecules. *J Membr Sci*. 2008;325:166–175.
35. Roh IJ, Park SY, Kim JJ, Kim CK. Effects of the polyamide molecular structure on the performance of reverse osmosis membranes. *J Polym Sci Part B: Polym Phys*. 1998;36:1821–1830.
36. Freger V. Kinetics of film formation by interfacial polycondensation. *Langmuir*. 2005;21:1884–1894.
37. Rao AP, Joshi SV, Trivedi JJ, Devmurari CV, Shah VJ. Structure–performance correlation of polyamide thin film composite membranes: effect of coating conditions on film formation. *J Membr Sci*. 2003;211:13–24.
38. Roh IJ, Khare VP. Investigation of the specific role of chemical structure on the material and permeation properties of ultrathin aromatic polyamides. *J Mater Chem*. 2002;12:2334–2338.
39. Jin Y, Su Z. Effects of polymerization conditions on hydrophilic groups in aromatic polyamide thin films. *J Membr Sci*. 2009; 330:175–179.
40. Ghosh AK, Hoek EMV. Impacts of support membrane structure and chemistry on polyamide-polysulfone interfacial composite membranes. *J Membr Sci*. 2009;336:140–148.
41. Mehta GD, Loeb S. Internal polarization in the porous substructure of a semipermeable membrane under pressure-retarded osmosis. *J Membr Sci*. 1978;4:261–265.
42. Loeb S, Titelman L, Korngold E, Freiman J. Effect of porous support fabric on osmosis through a Loeb-Sourirajan type asymmetric membrane. *J Membr Sci*. 1997;129:243–249.
43. Gray GT, McCutcheon JR, Elimelech M. Internal concentration polarization in forward osmosis: role of membrane orientation. *Desalination*. 2006;197:1–8.
44. McCutcheon JR, McGinnis RL, Elimelech M. Desalination by ammonia-carbon dioxide forward osmosis: influence of draw and feed solution concentrations on process performance. *J Membr Sci*. 2006;278:114–123.
45. McCutcheon JR, Elimelech M. Influence of concentrative and dilutive internal concentration polarization on flux behavior in forward osmosis. *J Membr Sci*. 2006;284:237–247.
46. McCutcheon JR, Elimelech M. Modeling water flux in forward osmosis: implications for improved membrane design. *AIChE J*. 2007;53:1736–1744.
47. Steuck MJ. *Porous membrane having hydrophilic surface and process*, Millipore Corporation, US Patent 4,618,533 (1986).
48. Singh S, Khulbe K, Matsuura T, Ramamurthy P. Membrane characterization by solute transport and atomic force microscopy. *J Membr Sci*. 1998;142:111–127.
49. Wang KY, Matsuura T, Chung TS, Guo WF. The effects of flow angle and shear rate within the spinneret on the separation performance of poly (ethersulfone) (PES) ultrafiltration hollow fiber membranes. *J Membr Sci*. 2004;240:67–79.
50. Lonsdale HK, Merten U, Riley RL. Transport properties of cellulose acetate osmosis membranes. *J Appl Polym Sci*. 1965;9:1341–1362.
51. Loeb S, Mehta GD. A two-coefficient water transport equation for pressure-retarded osmosis. *J Membr Sci*. 1979;4:351–362.
52. Song Y, Liu F, Sun B. Preparation, characterization, and application of thin film composite nanofiltration membranes. *J Appl Polym Sci*. 2005;95:1251–1261.
53. Roh IJ, Greenberg AR, Khare VP. Synthesis and characterization of interfacially polymerized. *Desalination*. 2006;191:279–290.
54. William A, Phillip WA, Yong JS, Elimelech M. Reverse draw solute permeation in forward osmosis: modeling and experiments. *Environ Sci Technol*. 2010;44:5170–5176.

Manuscript received Dec. 2, 2010, and revision received Feb. 15, 2011.